Nano Research
DOI 10.1007/s12274-014-0665-y
Research Article
ISSN 1998-0124
CN 11-5974/O4

Crystal-oriented wrinkles with origami-type junctions in few-layer hexagonal boron nitride

Camilla K. Oliveira[1,†], Egleidson F. A. Gomes[1], Mariana C. Prado[1], Thonimar V. Alencar[1], Regiane Nascimento[1], Leandro M. Malard[1], Ronaldo J. C. Batista[2], Alan B. de Oliveira[2], Helio Chacham[1], Ana M. de Paula[1], and Bernardo R. A. Neves[1] (✉)

[1] *Departamento de Física, ICEx, Universidade Federal de Minas Gerais – UFMG, C.P. 702, 30123-970 – Belo Horizonte, Brazil*
[2] *Departamento de Física, ICEB, Universidade Federal de Ouro Preto – UFOP, 35400-000 – Ouro Preto, Brazil*
[†] *Present address: Departamento de Física, Universidade Federal do Paraná – UFPR, Caixa Postal 19044, 81531-990 – Curitiba, Brazil*

Received: 5 September 2014
Revised: 20 November 2014
Accepted: 30 November 2014

KEYWORDS
hexagonal boron nitride,
2D materials,
wrinkles,
origami folding,
annealing

ABSTRACT

Understanding layer interplay is the key to utilizing layered heterostructures formed by the stacking of different two-dimensional materials for device applications. Boron nitride has been demonstrated to be an ideal substrate on which to build graphene devices with improved mobilities. Here we present studies on the morphology and optical response of annealed few-layer hexagonal boron nitride flakes deposited on a silicon substrate that reveal the formation of linear wrinkles along well-defined crystallographic directions. The wrinkles formed a network of primarily threefold and occasionally fourfold origami-type junctions throughout the sample, and all threefold junctions and wrinkles formed along the armchair crystallographic direction. Furthermore, molecular dynamics simulations yielded, through spontaneous symmetry breaking, wrinkle junction morphologies that are consistent with both the experimental results and the proposed origami-folding model. Our findings indicate that this morphology may be a general feature of several two-dimensional materials under proper stress-strain conditions, resulting in direct consequences in device strain engineering.

1 Introduction

On the macroscale, most materials, regardless of their dimensionality (one, two, or three), demonstrate conventional stress-strain behavior: They shrink upon compression (compressive stress) and expand upon extension (tensile stress) [1]. In particular, when two-dimensional (2D) or three-dimensional (3D) structures are under one-dimensional (1D) stress, they normally expand (or shrink) in the direction of a tensile (or compressive) stress, while shrinking (or expanding) in a perpendicular direction [1]. Auxetic (or possessing

Address correspondence to bernardo@fisica.ufmg.br

a negative Poisson's ratio) materials represent a deviation from such standard behavior, as they may simultaneously expand in both the parallel and perpendicular directions under 1D tensile stress [2]. As the length decreases towards the micro- and nanoscales, additional non-standard stress-strain behaviors may appear, such as negative compressibility (both static [3] and dynamic [4]), including an immense negative compressibility which arises from an immense positive compressibility [5].

In particular, materials based on 2D systems display a wide variety of physical and chemical properties, leading to a myriad of studies [6–14]. Due to the layered nature of such systems, the formation of wrinkles upon compressive stress could initially be perceived as an ordinary strain configuration [6–10]. However, both strain and strain gradients are known to alter fundamental physical properties of 2D materials, such as the "pseudomagnetic" quantum Hall effect in graphene [15], strain photonics in MoS_2 [16], and flexoelectricity in hexagonal boron nitride (h-BN) [17]. Consequently, a new term, *straintronics*, has been coined for this promising field [6–10, 14, 18]. Therefore, the formation of wrinkles in 2D materials is not described by ordinary or wrinkle engineering, but is a direct consequence of strain engineering, and may represent a major topic for further investigation. For graphene (the most investigated 2D material), its wrinkle formation, characterization, and application have already been subjects of intense study [6–10, 14]. The recently proposed massive fabrication of graphene nanoribbons represents just one example [19]. Therefore, in this investigation, a new non-conventional stress-strain behavior of 2D materials was revealed: The formation of crystallographically oriented origami-type wrinkles in annealed h-BN layers. Using atomic force microscopy (AFM), self-assembly procedures, and second harmonic generation (SHG) experiments, both the morphology and orientation of such wrinkles were studied. A simple phenomenological model and molecular dynamics simulations account for the wrinkle formation mechanism, which indicates that it could be a general feature of several 2D materials under proper stress-strain (or wrinkle engineering) conditions.

2 Results

2.1 AFM characterization of annealed h-BN

Figure 1 summarizes the morphological AFM characterization of annealed h-BN flakes and shows topographic images of a few-layer h-BN flake in three different magnifications. The small squares in Figs. 1(a) and 1(b) indicate the regions in which Figs. 1(b) and 1(c) were acquired, respectively. It is evident from Fig. 1 that the annealing treatment produced a well-defined geometric pattern of wrinkles.

In addition, the wrinkle orientation was not random, but rather occurred only at certain angles. As evidenced by their respective fast-Fourier transform (FFT) images (insets of Figs. 1(a) and 1(b)), there are mainly three

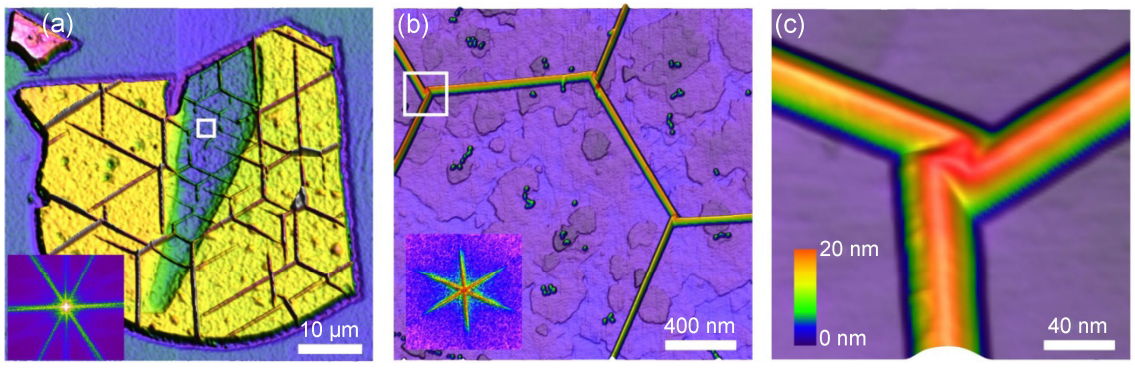

Figure 1 AFM characterization of h-BN flakes after annealing. (a) A 10-nm-thick flake displaying an orientationally ordered wrinkle pattern. The inset at the bottom left shows the FFT image of the flake topography. (b) Zoomed-in AFM image acquired in the region marked by a white square in (a). The wrinkle pattern orientation is evidenced by the FFT image at the bottom left of the figure. (c) Detailed topographic image of the wrinkle junction indicated by the white square in (b). The color scale at the bottom left of the image indicates the height variation.

orientations for the wrinkles in Fig. 1. A quick inspection of this figure reveals that the vast majority of wrinkle junctions are threefold, and Figs. 1(b) and 1(c) show more detailed images of such junctions. Each wrinkle in Fig. 1(c) is around 10-nm high, as indicated by the color scale, but, in general, the wrinkle height in all the investigated samples varied from a single nanometer to several tens of nanometers. An interesting feature of Fig. 1(c) is the morphology of a typical junction: The wrinkles always connect to each other through the vertices of a small, rotated triangle (indicated by the reddish shade in the center of the image).

2.2 Phosphonic acid decoration

An immediate question, which arises from the results in Fig. 1, is whether there is any relationship between the wrinkle orientation and the h-BN lattice. In other words, are the wrinkles crystallographically oriented? Two independent experimental procedures were employed to answer this question: (i) Decoration of h-BN with self-assembled octadecylphosphonic acid (OPA) molecules, and (ii) polarization-dependent SHG experiments. Recently, Prado et al. [20] demonstrated that decoration of graphene with OPA self-assembled monolayers enabled the identification of its crystallographic orientation. OPA is a 2.5-nm-long molecule with a phosphonic acid headgroup attached to a long linear alkyl chain. It self-assembles on graphene with its axis parallel to the surface, in a configuration that allows the headgroup of adjacent molecules to interact via hydrogen bonding, forming rippled domains which can be detected by AFM [20]. *Ab initio* calculations and AFM images showed that these ripples were oriented along the graphene armchair direction [20]. Since h-BN also has a hexagonal lattice, similar to that of graphene, with a lattice mismatch of only 1.7% [21], this same behavior should also be expected in an h-BN–OPA system. Therefore, *ab initio* calculations were performed to investigate the relative stability of OPA self-assembled monolayers (SAMs) atop h-BN, assuming that the OPA alkyl chains were oriented along either the armchair or zigzag directions. The calculations were based on density functional theory [22] within the local density approximation of the exchange-correlation functional, as implemented in the SIESTA method [23]. The same computational methodology, as was used in the previous study of OPA molecules atop graphene, was adopted here [20]. Concomitantly, h-BN flakes were decorated with OPA SAMs and were investigated via AFM imaging [20].

Figure 2 summarizes the results of both the theoretical calculations and experiments. Figures. 2(a) and 2(b) depict the optimized geometries (top and side views) for the most stable OPA SAM configuration on h-BN. The calculations indicated that OPA alkyl chains oriented along the zigzag direction of h-BN represent the most stable configuration, with formation energy per OPA dimer being 2.76 eV, smaller than that of chains oriented along the armchair direction.

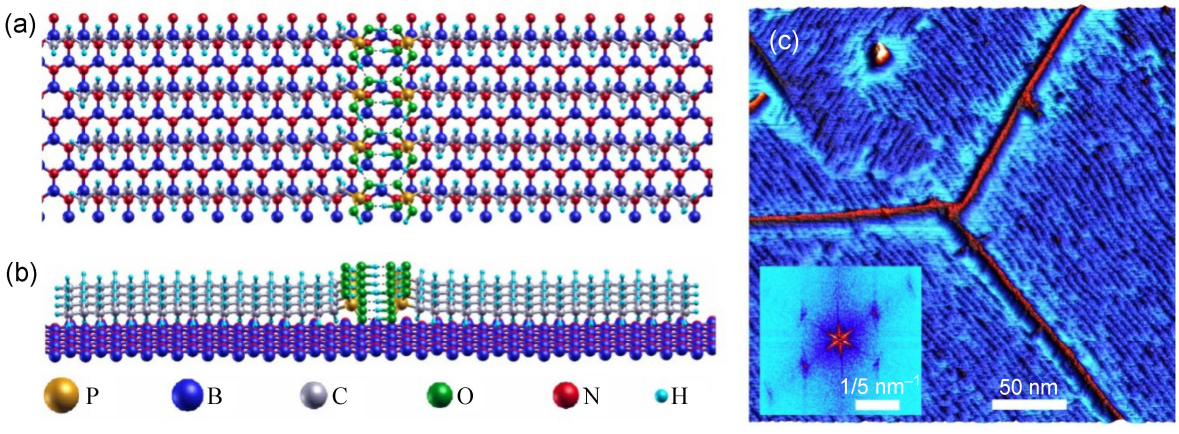

Figure 2 Theoretical and experimental investigation of OPA self-assembly on h-BN. (a) and (b) Detailed views ((a) top view, (b) side view) of the most stable OPA structure atop h-BN obtained from the calculations. (c) AFM-phase image of an annealed h-BN flake decorated with OPA SAMs which form parallel ripples across the sample surface (flake thickness = 8 nm). The inset shows the FFT image of the same region, evidencing the periodicity and orientation of the ripples.

Consequently, the ripples formed by OPA headgroups should be oriented along the armchair direction (see Fig. 2(a)). Figure 2(c) shows an AFM-phase image of an annealed few-layer h-BN flake completely covered by an OPA monolayer. A characteristic threefold wrinkle junction is evident in this image (indicated in red), along with minor wrinkles on the top left. This image also shows ripples (indicated in black) formed by the well-ordered phosphonic acid dimers. The FFT image (inset, bottom left) clearly reveals the 5-nm periodicity of these ripples, as expected from the *ab initio* results. These ripples are parallel to the wrinkle at the bottom right of Fig. 2(c) and form a 60° angle with the other two wrinkles. Since ripples should be oriented along the armchair direction of h-BN, the wrinkles should also be oriented along the same direction. A careful inspection of the top left of Fig. 2(c) reveals some ripple domains in an apparently different orientation. However, these ripples form a 120° angle with the dominant ripple domain and therefore, due to the C_3 symmetry of the system, are in the same armchair orientation. To summarize, the OPA self-assembly investigations (both theoretical and experimental) clearly indicate that the wrinkles formed on annealed h-BN are crystallographically oriented along its armchair direction.

2.3 Second harmonic generation experiments

In order to verify the above statement further, the wrinkle crystallographic orientation was studied by polarization-dependent second harmonic generation (SHG) microscopy. For h-BN, the odd-layer samples are characterized by D_{3h} point group symmetry, and the second-order susceptibility tensor has a single non-zero element [24, 25]. Thus, the generated second harmonic intensity as a function of the sample angle for a pump laser polarization ($\hat{e}_\omega$) parallel to the analyzer ($\hat{e}_{2\omega}$) is given as

$$I(2\omega) = I\cos^2(3\Phi + \Phi_0) \quad (1)$$

where Φ is the angle between the input laser polarization and the armchair direction, and Φ_0 is the initial crystallographic orientation of the h-BN sample.

Figures 3(a) and 3(b) show, respectively, the AFM and SHG images of an annealed h-BN flake with several wrinkles. In Fig. 3(b), brighter colors indicate stronger SHG intensity. A quick comparison between Figs. 3(a) and 3(b) indicates that the SHG signal is stronger at the wrinkles than at the flat regions of the flake. The intensity is proportional to the wrinkle height, which in turn depends on the increase in stress. We measured SHG images while rotating the sample (see sketch in the inset of Fig. 3(b)), and Fig. 3(c) shows the polar plot of the SHG intensity along the wrinkles as a function of the sample rotation angle Φ. The dots represent the measured data, and the red line is a fit of the data to Eq. 1 with $\Phi_0 = 0$, which clearly shows that the wrinkles are along the armchair direction. The measured intensity polar plot for all the wrinkles is displayed in Fig. 3(b), which

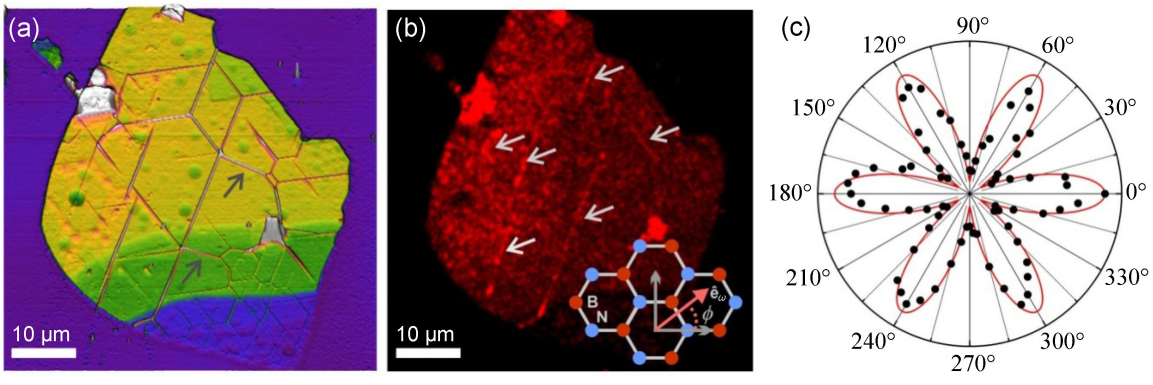

Figure 3 Second harmonic generation characterization of wrinkles. (a) AFM image of a 28-nm-thick h-BN flake after annealing, showing several wrinkles. The grey arrows indicate two wrinkles in non-armchair orientations. (b) SHG image of the same h-BN flake, brighter colors indicating stronger SHG intensity. Arrows indicate several wrinkles, which yield large SHG signals. The inset on the bottom right shows a sketch of the h-BN structure, indicating the angle between the laser polarization and the armchair direction *x*. (c) Polar plot of the SHG intensity along the wrinkles as a function of the sample rotation angle.

reveals that they all have the same dependence. Additionally, the plotted intensity along the sides of each wrinkle shows the same dependence, indicating that the domains are oriented at a 60° angle with respect to each other. In this sample, two wrinkles are not in the armchair direction (see grey arrows in Fig. 3(a)). Thus, as expected, they do not appear in the SHG image (Fig. 3(b)). Another interesting result from the SHG measurements is that the h-BN flake sits flat on top of the Si substrate with well-oriented wrinkles, but without any compressive or tensile stress on the flat part of the flake. The strain occurs only at the wrinkles and in their immediate vicinity.

3 Discussion

3.1 Phenomenological origami-like model and molecular dynamics simulations

It is a well-known fact that h-BN has an atomically flat surface, and for this reason, it is used as a substrate for graphene-based devices, since it increases carrier mobility by suppressing graphene undulations [21]. So, why should this crystallographic wrinkling occur? A possible reason lies in the annealing treatment and the difference between the thermal expansion coefficients of h-BN and the Si substrate, with a mechanism similar to that which causes graphene wrinkling on CVD-grown and mechanically exfoliated flakes [6–10, 14]. However, there is a subtle difference: While Si behaves as a standard material with a positive thermal expansion coefficient [1], h-BN displays anisotropic behavior. Along the *c*-axis of h-BN, the linear thermal expansion coefficient is positive, and, thus, it behaves as a standard material along this axis. However, in the plane, the thermal expansion coefficient is negative [26]. Consequently, h-BN layers shrink upon heating, while Si expands; on the other hand, during the cooling phase, h-BN expands, while the substrate shrinks. Therefore, since the substrate anchors the flakes, it causes a tensile stress upon heating, flattening the flakes, and causes a compressive stress upon cooling, wrinkling them. In other words, the observed wrinkles directly result from 2D compressive stress applied to the h-BN flakes by the Si substrate during the cooling phase of the annealing treatment. The physical mechanism is essentially identical to that proposed for graphene wrinkling, but with two distinctions: The difference between the thermal expansion coefficients of the graphene and substrate, and the absence of any reported observation of crystallographically oriented wrinkles in graphene so far [6–10, 14]. A straightforward verification of such a hypothesis is the direct comparison between the sum of wrinkle heights and the expected difference in thermal expansion between the Si substrate and h-BN flake. For example, we consider the h-BN flake of Fig. 1(a), which is roughly 50-μm long in any direction ($L \approx 50$ μm). Any arbitrary line profile in this flake will cross several wrinkles. Adding the heights of the crossed wrinkles yields the total wrinkle height H_W. Simultaneously, during the annealing process, the thermal expansion difference (E_{th}) between the Si substrate and h-BN flake is simply $E_{th} = L\,(\alpha_{Si} - \alpha_{BN})\,\Delta T$, where α_{Si} and α_{BN} are the thermal coefficients of Si and h-BN, respectively, and ΔT is the temperature variation in the annealing process. In any arbitrary line profile, we observe the approximate relationship $E_{th} \geqslant 2H_W$, which is a good indication that wrinkles are created via the mechanism proposed above.

In order to create such a well-organized and crystallographically oriented pattern of wrinkles, one would expect that the cooling phase (or stress application) should be conducted as slowly as possible, allowing the system to achieve its lowest energy configuration. Indeed, crystallographic wrinkles are only observed when the annealing treatment consists of a rapid heating step followed by a slow cooling step. For example, effective heating and cooling rates for production of crystallographic wrinkles are 50 and 8 °C/min, respectively. If faster cooling rates are employed, only conventional, non-crystallographic, and randomly oriented wrinkles are produced (Fig. S1 in the Electronic Supplementary Material (ESM)). A detailed investigation of the optimum heating and cooling rates for crystallographic wrinkle production, including those of other 2D materials [27], is out of the scope of the present work and represents the next step forward in this ongoing investigation.

If a uniform 2D compressive stress on an h-BN sheet induces the formation of crystallographic wrinkles, then the wrinkles may be described by an origami-

type folding pattern. Figure 4 presents a viable model for the origami-type formation of precisely oriented wrinkle junctions. Figure 4(a) shows a schematic of a feasible origami-folding pattern. The black lines in Fig. 4(a) indicate regions in which folds may occur, and their intersections form small triangles, which represent the unit cells of such an origami pattern. The shaded regions in Fig. 4(a) indicate three wrinkles (and their junction) which spontaneously formed when a 2D compressive stress was slowly applied to the sheet. As indicated by Figs. 4(b), 4(c), and 4(d), the model in Fig. 4(a) applies to h-BN, predicting wrinkle heights and origami patterns in a variety of sizes (larger than ~0.8 nm). Figure 4(e) illustrates the smallest possible wrinkle origami, which is formed by the small triangular unit cells of Fig. 4(b). In other words, the model in Fig. 4 predicts crystallographically oriented size-scalable wrinkles with triangle-shaped origami junctions. The striking similarities between the model in Fig. 4 and the AFM image in Fig. 1(c), including the C_3 symmetry of the junction, strongly support the assumption that the observed wrinkles are indeed result from origami-type folding of the h-BN sheet under 2D compressive stress.

Even though the vast majority of wrinkles occur in the armchair direction, it is possible to find a few wrinkles in the zigzag direction, such as the topmost one indicated in Fig. 3(a), and even some wrinkles that are oriented along neither the armchair nor zigzag directions. The model of Fig. 4 can be modified so that its triangular unit cells present a zigzag edge. In addition, in the continuum limit, Fig. 4(a) is consistent with wrinkles in any orientation. In that case, what is it that makes armchair-oriented wrinkles so much more frequent than zigzag ones? In principle, the reason might lie in either the folding energetics or the dynamics, although it remains to be explained. Nevertheless, such armchair-versus-zigzag occurrence is a topic of interest in hexagonal 2D material research. For example, it was recently observed that tearing monolayer graphene produces essentially zigzag- and armchair-oriented edges, the latter being more common [28].

Finally, in order to verify the validity of the origami-like model of Fig. 4, molecular dynamics simulations, utilizing a periodic supercell approach, were carried out for a biaxially compressed h-BN layer atop an unstrained h-BN surface. As an initial condition, shown in Fig. 5(a), shallow ripples were imposed, forming a honeycomb superlattice akin to the wrinkle structure of Fig. 1(b). As time evolved in the simulation (see the video in the ESM), the wrinkle structure increased in height and modified its shape, and the compressive strain of the planar part of the BN layer was gradually relaxed. The final, stable wrinkle structure (after 120 ps) is shown in Fig. 5(b). The final junction structure shows the characteristic rotated-triangle shape seen in both the experimental morphology (Fig. 1(c)) and the origami model of Fig. 4.

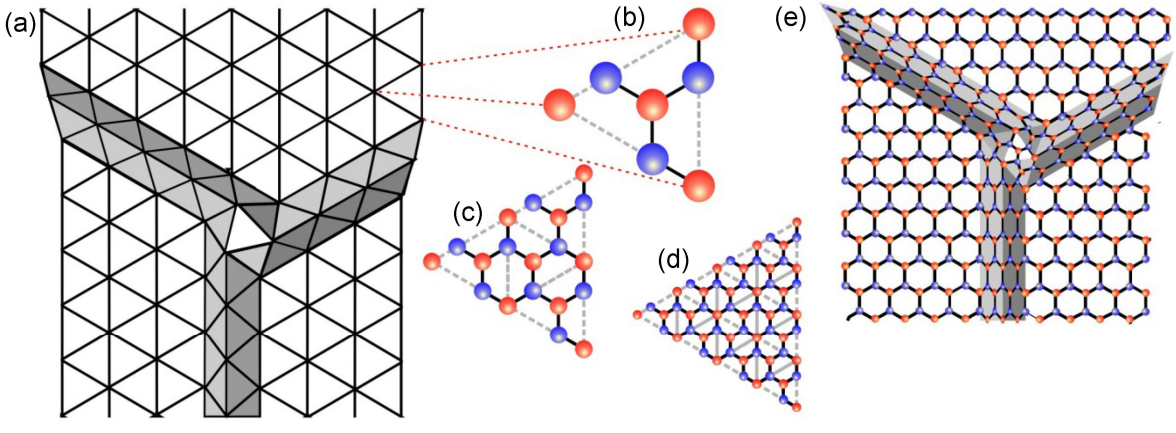

Figure 4 The origami-like model for the wrinkle junctions. (a) Schematic of the proposed origami-like folding of an h-BN sheet. The unit cell in this model is a triangle, which can be scaled to a variety of sizes, as indicated by (b), (c), and (d). (e) Proposed model for the smallest possible h-BN wrinkle junction; the wrinkles are along the armchair direction and their junction forms a small triangle at the center.

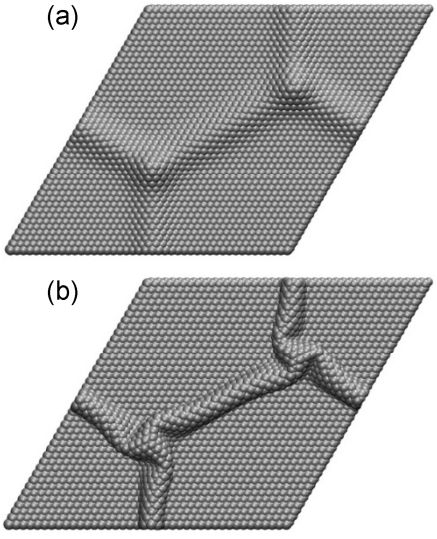

Figure 5 Molecular dynamics simulations of wrinkle junction formation. (a) Initial top-layer configuration used for MD simulations of a biaxially compressed BN layer atop a fixed, unstrained layer (not shown). (b) Final, stable wrinkle structure obtained after 120 ps (or 6 million MD steps). Note the spontaneous symmetry breaking from the initial to final states of the wrinkle junction, from C_{3v} to C_3, respectively, and its rotated triangular morphology.

It is noteworthy that the spontaneous symmetry breaking, which occurred during the molecular dynamics simulation, is consistent with the experimental results. The symmetry of the initial ripple junction, as shown in Fig. 5(a), was C_{3v}, with mirror symmetry along the long diagonal plane of the cell (which is along the armchair direction). The symmetry of the final wrinkle junction, as shown in Fig. 5(b), was C_3, without such mirror symmetry. The latter is, in fact, the symmetry of the experimental wrinkle junctions. Therefore, the mechanical characteristics of h-BN allow for the spontaneous formation of origami-type structures in response to biaxial compression.

4 Conclusions

In conclusion, this work reported on origami-type wrinkles created on h-BN through a straightforward strain engineering procedure, viz., thermally induced progressive application of 2D compressive stress. In other words, origami-type folding and wrinkling might be general properties of any 2D material, if proper strain engineering conditions are applied. Hexagonal-lattice 2D materials, such as h-BN and graphene, should present the same origami pattern [27], whereas different surface lattices, such as those of 2D chalcogenides (encompassing metals, semiconductors, and topological insulators such as MoS_2, WS_2, $MoTe_2$, Bi_2Se_3, and others), could yield topologically different origami patterns. Such wrinkle engineering could ultimately be used to generate and control new "pseudomagnetic," flexoelectric, and photonic effects on specific 2D materials.

5 Experimental section

Sample preparation and AFM characterization: The h-BN flakes were prepared by standard mechanical exfoliation, using commercial h-BN powder (Sigma-Aldrich) [29]. The exfoliated flakes were transferred onto a Si substrate doped with a thin layer (300 nm) of silicon oxide, and annealed at 1,000 °C for 25 min in a quartz tube. The heating and cooling rates for crystallographic wrinkle production were 50 and 8 °C/min, respectively. AFM characterization of the samples was carried out on Bruker MultiMode 8 and Park XE-70 microscopes operating in PeakForce and intermittent contact modes, respectively. Si cantilevers (from Bruker, Mikromasch and Nanosensors), with spring constants of 0.5–40 N/m and tip radius of curvature ~10 nm, were employed throughout the study for sample imaging.

Second harmonic generation experiments: The SHG microscopy system used a 140-fs Ti-sapphire laser, which was directed to a confocal scanning laser microscope modified for two-photon excitation. The laser (λ = 800 nm) was focused on the sample at normal incidence by a 40× objective. The SH back-reflected signal at 400 nm was collected by the same objective. It was then directed by a dichroic mirror to a thin bandpass filter (20 nm) centered at the SH wavelength, a polarizer analyzer, and finally detected by a photo-multiplier tube. The sample was mounted on a rotation stage for the polarization dependence measurements.

Molecular dynamics simulations: The molecular dynamics (MD) technique, as implemented in the Large-scale Atomic/Molecular Massively Parallel Simulator (LAMMPS) package [30], was used to simulate an h-BN bilayer in the canonical ensemble. The bottom layer, representing the unstrained h-BN

surface, consisted of a 40 × 40 periodic supercell of 3,200 atoms. Those atoms were not subject to strain, and the resultant forces on them were set to zero in all simulations. The strained h-BN upper layer was represented by a 44 × 44 supercell of 3,872 atoms, biaxially compressed by 1/11, such that its lattice vectors coincided with those of the unstrained h-BN surface. In the initial condition, shown in Fig. 5(a), shallow ripples were imposed by increasing the *z*-coordinates of the B and N atoms in a Gaussian profile, forming a honeycomb superlattice akin to the wrinkle structure of Fig. 1(b). For the interactions between atoms, we used the Tersoff potential [31] with parameters given by Albe and Möller [32]. In addition to the Tersoff potential, a force field acting on each atom, perpendicular to and directed towards the h-BN surface, was considered to represent the van der Waals interactions between the planes. Such a force field is given by $F = 4a \cdot d^{-5}$ [33], where d is the distance from the plane that contains the atoms of the bottom layer, and $a = 4.3$ eV·Å^4. The temperature was maintained at 10 K by a Nosé–Hoover thermostat [34, 35]. The time-step was 0.0002 ps, and the total simulation time was 120 ps (or 6 million MD steps).

Acknowledgements

The authors are thankful to Prof. Rodrigo Gribel for the use of the laboratory facilities. All authors acknowledge financial support from Coordenação de Aperfeiçoamento de Pessoal de Nível Superior (Capes), Conselho Nacional de Desenvolvimento Científico e Tecnológico (CNPq), Fundação de Amparo à Pesquisa do estado de Minas Gerais (Fapemig), Rede Nacional de Pesquisa em Nanotubos de Carbono, and Instituto Nacional de Ciência e Tecnologia (INCT-Nano-Carbono).

Electronic Supplementary Material: Supplementary material (AFM images of h-BN flakes submitted to fast cooling treatments illustrating conventional, non-organized wrinkles, and the video showing the time-evolution of h-BN wrinkles in molecular dynamics simulations) is available in the online version of this article at http://dx.doi.org/10.1007/s12274-014-0665-y.

References

[1] Bower, A. F. *Applied Mechanics of Solids*; CRC Press: Florida, 2009.

[2] Lakes, R. Foam structures with a negative Poisson's ratio. *Science* **1987**, *235*, 1038–1040.

[3] Baughman, R. H.; Stafstrom, S.; Cui, C.; Dantas, S. O. Materials with negative compressibilities in one or more dimensions. *Science* **1998**, *279*, 1522–1524.

[4] Barboza, A. P. M.; Chacham, H.; Oliveira, C. K.; Fernandes, T. F. D.; Martins Ferreira, E. H.; Archanjo, B. S.; Batista, R. J. C.; de Oliveira, A. B.; Neves, B. R. A. Dynamic negative compressibility of few-layer graphene, h-BN, and MoS_2. *Nano Lett.* **2012**, *12*, 2313–2317.

[5] Cairns, A. B.; Catafesta, J.; Levelut, C.; Rouquette, J.; van der Lee, A.; Peters, L.; Thompson, A. L.; Dmitriev, V.; Haines, J.; Goodwin, A. L. Giant negative linear compressibility in zinc dicyanoaurate. *Nat. Mater.* **2013**, *12*, 212–216.

[6] Obraztsov, A. N.; Obraztsova, E. A.; Tyurnina A. V.; Zolotukhin, A. A. Chemical vapor deposition of thin graphite films of nanometer thickness. *Carbon* **2007**, *45*, 2017–2021.

[7] Li, X.; Cai, W.; An, J.; Kim, S.; Nah, J.;Yang, D.; Piner, R.; Velamakanni, A.; Jung, I.; Tutuc, E.; Banerjee, S. K.; Colombo, L.; Ruoff, R. S. Large-area synthesis of high-quality and uniform graphene films on copper foils. *Science* **2009**, *324*, 1312–1314.

[8] Xu, K.; Cao, P.; Heath, J. R. Scanning tunneling microscopy characterization of the electrical properties of wrinkles in exfoliated graphene monolayers. *Nano Lett.* **2009**, *9*, 4446–4451.

[9] Robertson, A. W.; Bachmatiuk, A.; Wu, Y. A.; Schäffel, F.; Büchner, B.; Rümmeli, M. H.; Warner, J. H. Structural distortions in few-layer graphene creases. *ACS Nano* **2011**, *5*, 9984–9991.

[10] Zhu, W.; Low, T.; Perebeinos, V.; Bol, A. A.; Zhu, Y.; Yan, H.; Tersoff, J.; Avouris, P. Structure and electronic transport in graphene wrinkles. *Nano Lett.* **2012**, *12*, 3431–3436.

[11] Huang, Y.; Wu, J.; Xu, X.; Ho, Y.; Ni, G.; Zou1, Q.; Kok, G.; Koon, W.; Zhao, W.; Castro Neto, A. H.; Eda, G.; Shen, C.; Özyilmaz, B. An innovative way of etching MoS_2: Characterization and mechanistic investigation. *Nano Res.* **2013**, *6*, 200–207.

[12] Lherbier, A.; Roche, S.; Restrepo, O. A.; Niquet, Y. M.; Delcorte, A.; Charlier, J. C.; Highly defective graphene: A key prototype of two dimensional Anderson insulators. *Nano Res.* **2013**, *6*, 326–334.

[13] Shaw, J. C.; Zhou, H.; Chen, Y.; Weiss, N. O.; Liu, Y.; Huang, Y; Duan, X. Chemical vapor deposition growth of monolayer $MoSe_2$ nanosheets. *Nano Res.* **2014**, *7*, 511–517.

[14] Zhang, K.; Arroyo, M. Understanding and strain-engineering wrinkle networks in supported graphene through simulations. *J. Mech. Phys. Solids* **2014**, *72*, 61–74.

[15] Guinea, F.; Katsnelson, M. I.; Geim, A. K. Energy gaps and a zero-field quantum hall effect in graphene by strain engineering. *Nat. Phys.* **2010**, *6*, 30–33.

[16] Feng, J.; Qian, X.; Huang, C. W.; Li, J. Strain-engineered artificial atom as a broad-spectrum solar energy funnel. *Nat. Photon.* **2012**, *6*, 866–872.

[17] Naumov, I.; Bratkovsky, A. M.; Ranjan, V. Unusual flexoelectric effect in twodimensional noncentrosymmetric sp^2-bonded crystals. *Phys. Rev. Lett.* **2009**, *102*, 217601.

[18] Roy, K.; Bandyopadhyay, S.; Atulasimha, J. Hybrid spintronics and straintronics: A magnetic technology for ultra-low energy computing and signal processing. *Appl. Phys. Lett* **2011**, *99*, 063108.

[19] Pan, Z.; Liu, N.; Fu, L.; Liu, Z. Wrinkle engineering: A new approach to massive graphene nanoribbon arrays. *J. Am. Chem. Soc.* **2011**, *133*, 17578–17581.

[20] Prado, M. C.; Nascimento, R.; Moura, L. G.; Matos, M. J. S.; Mazzoni, M. S. C.; Cancado, L. G.; Chacham, H.; Neves, B. R. A. Two-dimensional molecular crystals of phosphonic acids on graphene. *ACS Nano* **2011**, *5*, 394–398.

[21] Dean, C. R.; Young, A. F.; Meric, I.; Lee, C.; Wang, L.; Sorgenfrei, S.; Watanabe, K.; Taniguchi, T.; Kim, P.; Shepard, K. L.; Hone, J. Boron nitride substrates for high-quality graphene electronics. *Nat. Nanotech.* **2010**, *5*, 722–726.

[22] Kohn, W.; Sham, L. J. Self-consistent equations including exchange and correlation effects. *Phys. Rev.* **1965**, *40*, A1133–A1138.

[23] Soler, J. M.; Artacho, E.; Gale, J. D.; Garcia, A.; Junquera, J.; Ordejon, P.; Sanchez-Portal, D. The SIESTA method for *ab initio* order-*n* materials simulation. *Condens. Matter* **2002**, *14*, 2745–2779.

[24] Malard, L. M.; Alencar, T. V.; Barboza, A. P. M.; Mak, K. F.; de Paula, A. M. Observation of intense second harmonic generation from MoS_2 atomic crystals. *Phys. Rev. B* **2013**, *87*, 201401.

[25] Li, Y.; Rao, Y.; Mak, K. F.; You, Y.; Wang, S.; Dean, C. R.; Heinz, T. F. Probing symmetry properties of few-layer MoS_2 and h-BN by optical second-harmonic generation. *Nano Lett.* **2013**, *13*, 3329–3333.

[26] Paszkowicz, W.; Pelka, J. B.; Knapp, M.; Szyszko, T.; Podsiadlo, S. Lattice parameters and anisotropic thermal expansion of hexagonal boron nitride in the 10–297.5 K temperature range. *Appl. Phys. A* **2002**, *75*, 431–435.

[27] Li, L. H.; Cervenka, J.; Watanabe, K.; Taniguchi, T.; Chen, Y. Strong oxidation resistance of atomically thin boron nitride nanosheets. *ACS Nano* **2014**, *8*, 1457–1462.

[28] Kim, K.; Artyukhov, V. I.; Regan, W.; Liu, Y.; Crommie, M. F.; Yakobson, B. I.; Zettl, A. Ripping graphene: Preferred directions. *Nano Lett.* **2012**, *12*, 293–297.

[29] Oliveira, C. K.; Matos, M. J. S.; Mazzoni, M. S. C.; Chacham, H.; Neves, B. R. A. Anomalous response of supported few-layer hexagonal boron nitride to DC electric fields: A confined water effect? *Nanotechnology* **2012**, *23*, 175703.

[30] Plimpton, S. J. Fast parallel algorithms for short-range molecular dynamics. *J. Comp. Phys.* **1995**, *117*, 1–19.

[31] Tersoff, J. New empirical approach for the structure and energy of covalent systems. *Phys. Rev. B* **1988**, *37*, 6991.

[32] Albe, K.; Möller, W. Modelling of boron nitride: Atomic scale simulations on thin film growth. *Comp. Mat. Sci.* **1998**, *10*, 111–115.

[33] Dappe, Y. J.; Basanta, M. A.; Flores, F.; Ortega, J. Weak chemical interaction and van der Waals forces between graphene layers: A combined density functional and inter-molecular perturbation theory approach. *Phys. Rev. B* **2006**, *74*, 205434.

[34] Nosé, S. A unified formulation of the constant temperature molecular dynamics methods. *J. Chem. Phys.* **1984**, *81*, 511.

[35] Hoover, W. G. Canonical dynamics: Equilibrium phase-space equations. *Phys. Rev. A* **1985**, *31*, 1695.

Table of contents

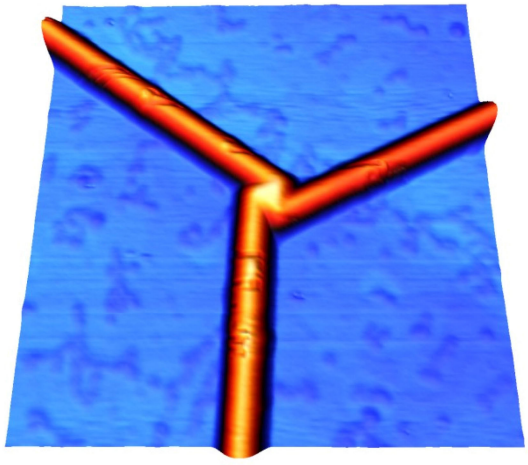

The morphology and optical response of heat-treated hexagonal boron nitride few-layer flakes reveal the formation of linear wrinkles along well-defined crystallographic directions. The wrinkles form a network of origami-type junctions throughout the sample, accommodating layer strain. The results indicate that this process may be a general feature of several 2D materials under proper stress-strain conditions, resulting in direct consequences on device strain engineering.

Electronic Supplementary Material

Crystal-oriented wrinkles with origami-type junctions in few-layer hexagonal boron nitride

Camilla K. Oliveira[1,†], Egleidson F. A. Gomes[1], Mariana C. Prado[1], Thonimar V. Alencar[1], Regiane Nascimento[1], Leandro M. Malard[1], Ronaldo J. C. Batista[2], Alan B. de Oliveira[2], Helio Chacham[1], Ana M. de Paula[1], and Bernardo R. A. Neves[1] (✉)

[1] *Departamento de Física, ICEx, Universidade Federal de Minas Gerais – UFMG, C.P. 702, 30123-970 – Belo Horizonte, Brazil*
[2] *Departamento de Física, ICEB, Universidade Federal de Ouro Preto – UFOP, 35400-000 – Ouro Preto, Brazil*
[†] *Present address: Departamento de Física, Universidade Federal do Paraná – UFPR, Caixa Postal 19044, 81531-990 – Curitiba, Brazil*

Supporting information to DOI 10.1007/s12274-014-0665-y

Sample quenching

Boron nitride samples were heated at a rate of 8 °C/min and were then quickly removed from the furnace. If faster cooling rates are employed, only conventional, non-crystallographic, and randomly oriented wrinkles are produced.

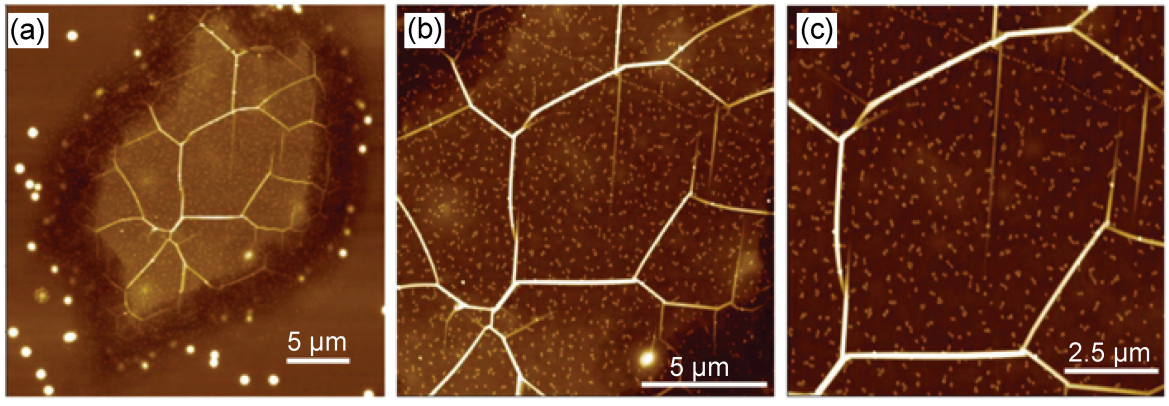

Figure S1 AFM characterization of few-layer h-BN flakes after slow annealing and quenching. (a) A flake showing a non-orientationally ordered wrinkle pattern. (b) Zoomed-in AFM image from image (a). (c) Zoomed-in AFM image from image (b).

Address correspondence to bernardo@fisica.ufmg.br